Multiplet Analysis at Coso Geothermal

by Jonathan M. Lees

Abstract We have searched the Coso geothermal field (CGF) for microseismicity in seismic doublets, co-located hypocenters that appear to have nearly identical waveforms. Using 1085 high-quality events from 1993 to 1994, we identified numerous doublets, some occurring within minutes of each other. We subdivided hypocentral data into spatial clusters to reduce the computational burden and evaluated multiple cross-correlation pairs, assigning scores to each pair. As an example, one spatial cluster includes 183 events yielding 96 high-correlation (>0.6) paired events. To isolate potential multiplets, equivalence class analysis and cluster analysis routines were used. Among the 96 high-correlation pairs, 24 equivalence classes have been isolated. While most of these are doublets, 8 classes include 3 or more cluster members and one class includes 16 members. Relative locations were calculated using phase shifts between corresponding events. Detailed analysis of hypocenter relocations shows elongate, vertical structure with apparent random temporal variations. The multiplets do not appear to be true repeating events; rather, they are clusters of small, nearly identically oriented ruptures, perhaps representing swarms of fractures activated by fluid-pressure fluctuations. Using the small volumes encompassing each multiplet, we estimate fracture densities measure between 0.02 and 0.4 m^{-1} and are largest near injection wells.

Introduction

The Coso geothermal field (CGF) is located east of the Sierra Nevada Batholith in a region exhibiting extensive volcanism and pervasive faulting associated with extensional tectonics of this province (Duffield and Bacon, 1981; Duffield et al., 1980; Roquemore, 1980). The CGF has a high rate of microseismicity, broadly dispersed and concentrated in the geothermal field, with a strong spatial and temporal correlation to production/injection well activity (Feng and Lees, 1998). Among the numerous events recorded daily, many appear to have similar waveforms. Events with such similar waveforms must occur in nearly the same position and share a similar source time function and mechanism. Two events that share these characteristics are called a simple earthquake doublet (Poupinet et al., 1984; for other studies using doublets, see also Haase et al., 1995; Fremont and Malone, 1987; Nadeau et al., 1994; Gillard, et al., 1996; Phillips et al., 1997). In the case of Coso, many sequences of events share such similar characteristics, and these are called multiplets, for multiple occurrences of nearly the same event. While the signals recorded from these events are nearly identical, they are not exactly the same. We may assume that such similar events occur along the same rupture plane, although they are not perfectly coincident. The variations in the signal may be attributed to variations along the fault and path effects for each event. With seismic multiplets, we can obtain detailed information about the nature, orientation, and time signature of ruptures in the geothermal field.

Feng and Lees (1998) found a direct correlation of microseismicity fluid injection and circulation in the Coso geothermal field. Isolated clusters can be partitioned within the field by variations of transpressional and transtensional regimes in the field, and the spatial clustering observed in maps of microseismicity is associated with distinct geologic blocks. Furthermore, the stress analysis shows that the Coso geothermal field seismicity is distinct from regional seismicity in its temporal and spatial distribution. Three-dimensional distribution of seismic parameters, such as attenuation (Wu and Lees 1996), is consistent with this scenario, where high attenuation zones correlate with high heat sources in the field. In this study, numerous doublets and multiplets from Coso are identified and quantified. Multiplets including nine or more similar events are relocated with high precision, and individual conduits or crack zones are delineated.

Data Selection and Doublet Search Method

The CGF data recording system consists of 16 active, short-period stations recording at 2 msec (480 samples/sec) sampling rate (Fig. 1). The data used in this article come from several clusters recorded on a high-frequency downhole network installed by the Navy Geothermal Office and CalEnergy Co. In the 1993 to 1995 period, more than 2500 high-quality events were recorded at more than eight stations

Figure 1. Areal view of Coso geothermal field showing the full station array. Lines represent mapped faults taken from the geology map of Duffield and Bacon (1981). Central gray-shade blobs are rhyolite domes. Well symbols indicate location of current production and injection wells. Several stations have the same coordinates with different names because they were changed after initial installation. (Generally, the depths of burial were modified after reinstallation.)

of the downhole array. These form the underlying database from which events chosen for this study are drawn. Events fall into several spatial clusters (Fig. 2) associated with fluid flow and stress distribution in the geothermal field (Feng and Lees, 1998).

The method used for finding doublets in the CGF follows that of Aster and Scott (1993). The area is partitioned into clusters where potential doublets are expected to be found, and each cluster is treated individually. Within each cluster, events are paired, common stations gathered, and time series extracted for a 2-sec window starting 0.1 sec before the P-wave arrival. Multiple-taper spectra (Lees and Park, 1995) were calculated, and for each pair of traces, cross-coherency and cross-correlation scores were generated. Correlation scores were defined as the median value of all the cross-correlated stations for each pair of events. Although both P and S-wave phase arrivals were employed in other parts of the analysis, only vertical seismograms were used for this selection process, for example, initial event location and source parameter estimation. The scores were then utilized in equivalence class analysis and cluster analysis routines to isolate groups of events that were close to each other but far from other groups.

An example suite of 17 vertical seismograms for a multiplet in group NE recorded at Station S1 (Fig. 1) is presented in Figure 3. Because the data used in this study were recorded on borehole seismometers, the signal-to-noise ratio is greater than 1 at relatively high frequency (Fig. 4).

The P-wave arrivals have been aligned by cross-correlation methods, although further visual adjustments were made for the purpose of fine tuning. In several instances within large multiplet sequences, cross-correlation techniques failed to provide accurate phase coherency, perhaps
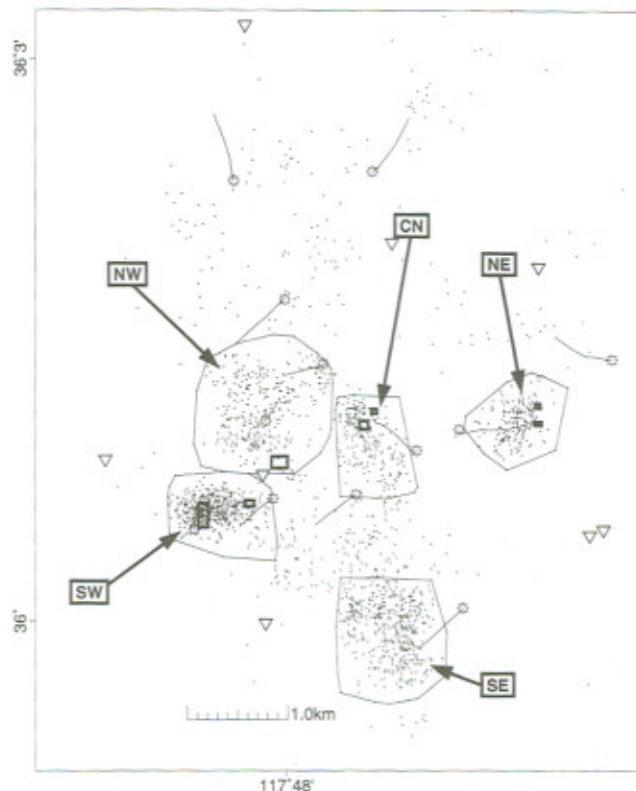

Figure 2. Plan view showing epicenter locations of events and initial clusters used for search. Cluster tags are labeled for identification in the text. Small rectangular boxes show targets and outlines of specific large multiplets (N > 9).
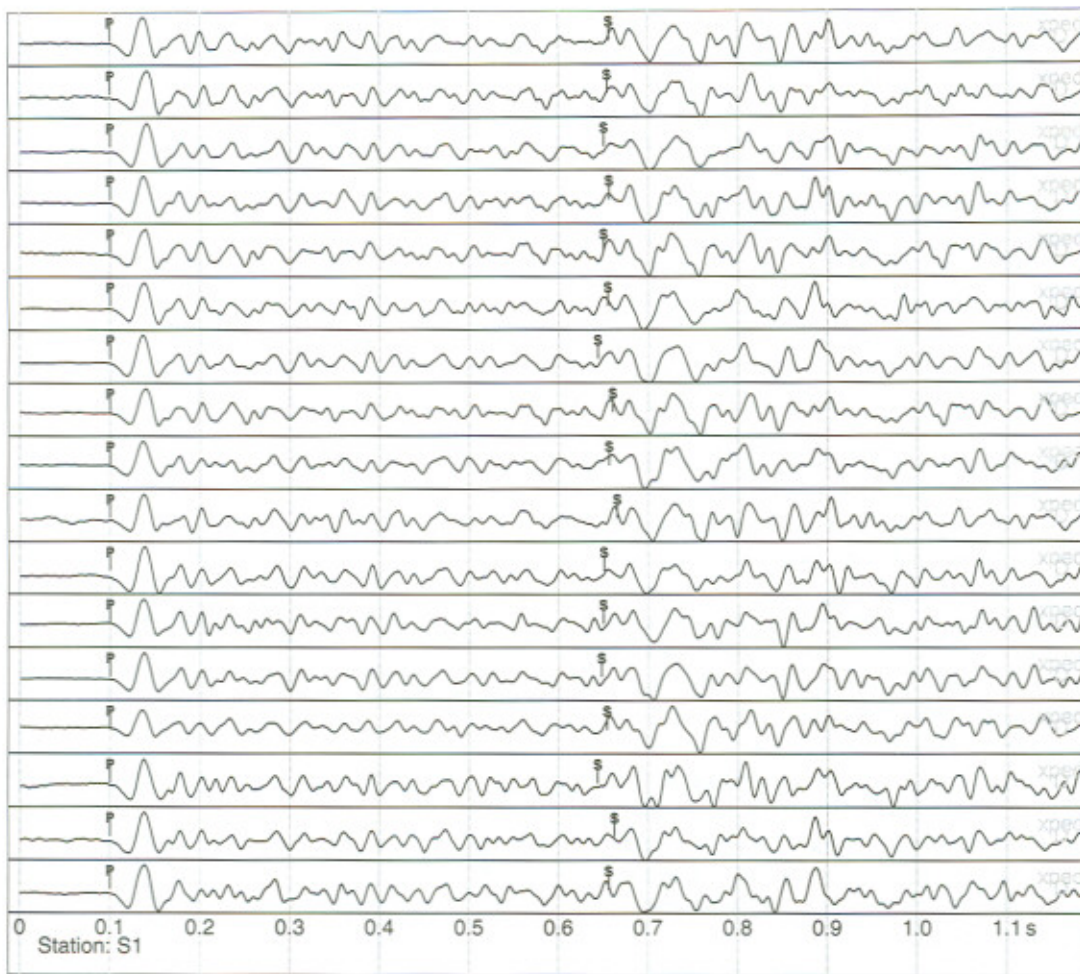
Figure 3. Vertical-component seismograms from one multiplet cluster recorded on station S1. Signals are aligned on the *P*-wave arrival time. *S*-wave arrivals, picked on horizontal components (not shown), are plotted for reference.
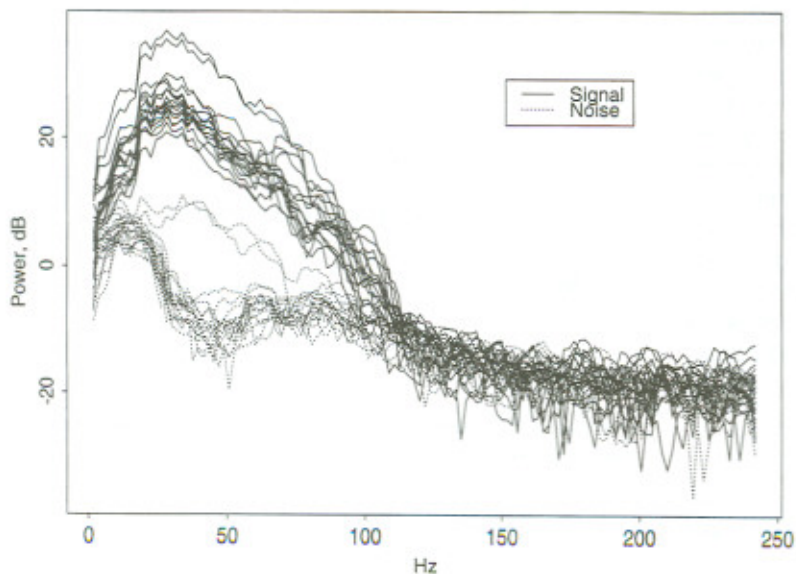

Figure 4. Signal and noise frequency spectra for 17 events in the NE1 cluster. The sampling rate is 480 samples/sec, and signal-to-noise ratio is greater that 1 out to 100 Hz.

due to excessive, sporadic noise, and alignment was done on specific phases observed across the whole sequence. [New software allowed the investigator to overlap and shift traces until the "best" correlation was achieved. Of course, "best" is an interpretation on the part of the investigator. Strict adherence to the quantitative cross-correlation phase shift excludes the possibility that, on occasion, the seismologist may use experience and, perhaps, bias in the determination of phase-shift data. See Phillips *et al.* (1997) for a short discussion of hand-picks over computer-picks.] *S*-picks are shown, although they are generally made on horizontal records. There is a strong correlation, wiggle for wiggle, on nearly all the traces. Naturally, there is some difference between events due to slight variations of source and path effects associated with variable location. The relocation procedure, described later, assumes that variations in source time functions and path effects are minimal, in that all phase shifts can be attributed to spatial offset of events.

In all, 792 events showed very high cross-correlation ($\rho > 0.8$) and equivalence class analysis produced clustering represented in Table 1. Sorted by cluster (Table 2), the northeast cluster (NE) had the smallest number of doublets, due to the relatively recent activation of an injection well in that area. The SW region had much more intense seismicity concentrated in a narrow zone. The diffuse cloud of seismicity in each of these clusters is due, in part, to errors in event location, as hypocenters typically have error ellipsoids on the order of 50 to 100 m for events carefully picked using cross-correlation methods. [Vidale *et al.* (1994) report errors of 10 m along the Calaveras fault.]

The time line showing the onset and end of each event multiplet is provided in Figure 5. Time lines are organized by cluster, so spatial variations can be observed. The multiplets in cluster 2 (NE sector) were initiated in October 1994, when a nearby well was installed and started (injection) operation. It is apparent that some doublets occurred over a considerable time span, including some cases where more than a year lapse time was observed between doublet events. In other cases, multiplets fractured within seconds, or minutes, of each other and represented a burst of activity in a localized area. These bursts likely correlate with injection activity and represent activation of faults induced by fluid injection/extraction. Figure 6 shows the distribution of 161 high-correlation doublet time intervals. The heavy preponderance of short time intervals is consistent with low-magnitude seismicity associated with high levels of fluid flow in the field. The extensive cross-faulting in the Coso region (Fig. 1; Roquemore, 1980; Duffield and Bacon, 1981) indicates that it is highly probable that these events lie on previously ruptured faults, which are simply reactivated during increased stress periods.

Relative Event Relocation

The relative timing procedure (Poupinet *et al.*, 1984) for a seismic doublet assumes that for two signals $s_1(t)$ and $s_2(t)$ the Fourier transforms are represented by

Table 1

Number of occurrences of multiplets of varying size using all the data in the Coso Geothermal field. The 17-event multiplet occurred in the NE cluster near an injection well.

Number per Multiplet	Number of Occurrences
2	149
3	64
4	30
5	9
6	6
8	1
9	1
10	2
11	1
12	3
17	1

Table 2

Distribution of multiplet events. First column is the total number of events selected for doublet search. Second column represents the number of different events that were found to be similar to at least one other event. The last column represents the number of different classes found for each cluster. These are combinations of doublet or multiplet events.

Cluster Tag	Number of Events	Number of Multiplets	Number of Classes
CN	252	137	40
NE	189	109	32
NW	335	110	39
SE	479	195	76
SW	525	241	80

$$S_1(f) = a_1 e^{i\phi_1}, \tag{1}$$

$$S_2(f) = a_2 e^{i\phi_2}, \tag{2}$$

where (a_1, a_2) are amplitudes and (ϕ_1, ϕ_2) are phases. For similar earthquakes, the phase shift is assumed to be a constant, so the time series are simply shifted by τ,

$$s_1 = k \cdot s_2(t + \tau), \tag{3}$$

where

$$k = a_1(f)/a_2(f) = \text{constant}, \tag{4}$$

with phase shift

$$\theta(f) = 2\pi \cdot \tau \cdot f \tag{5}$$

(f being the frequency). In the Fourier transform domain, this becomes

$$S_2(f) = \frac{1}{k} \cdot e^{-2\pi f \tau} \cdot S_1(f). \tag{6}$$

5 : hlist.SW

5:8

5:11

5:10

4 : hlist.SE

3 : hlist.NW

3:12

2 : hlist.NE

2:9

1 : hlist.CN

1:10

1:12

1:11

0	61	122	184	243	304	365	426	487	549

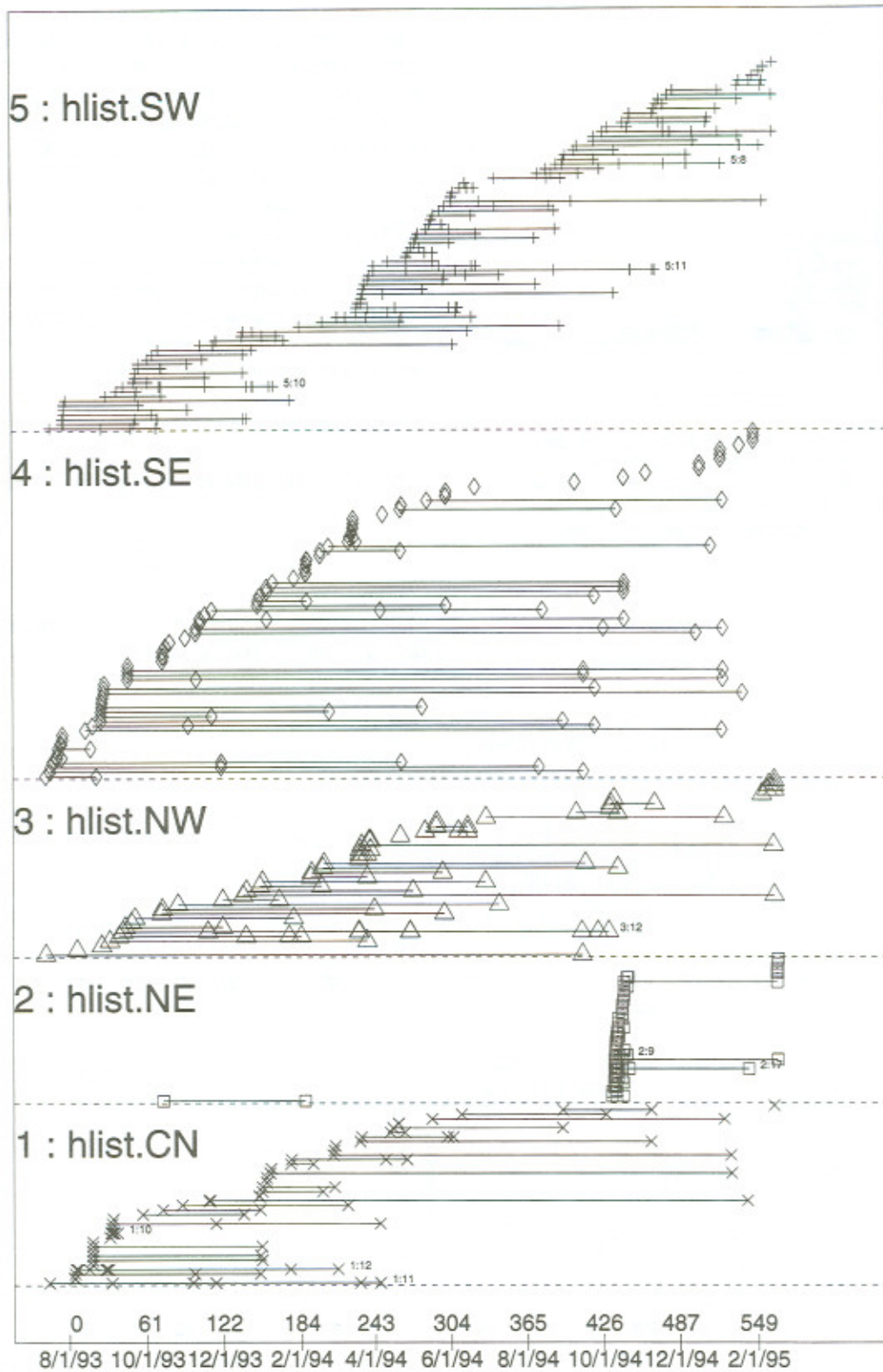8/1/93 10/1/93 12/1/93 2/1/94 4/1/94 6/1/94 8/1/94 10/1/94 12/1/94 2/1/95

Figure 5.   Time line of events. Each event is plotted as a number associated to its corresponding spatial cluster, where 1 = CN, 2 = NE, 3 = NW, 4 = SE, and 5 = SW. Vertical axis separates different doublet sequences. Large multiplets are emphasized by adding the number of events in the multiplet to the final event marker for the multiplet. There is a 17-event multiplet in NE.
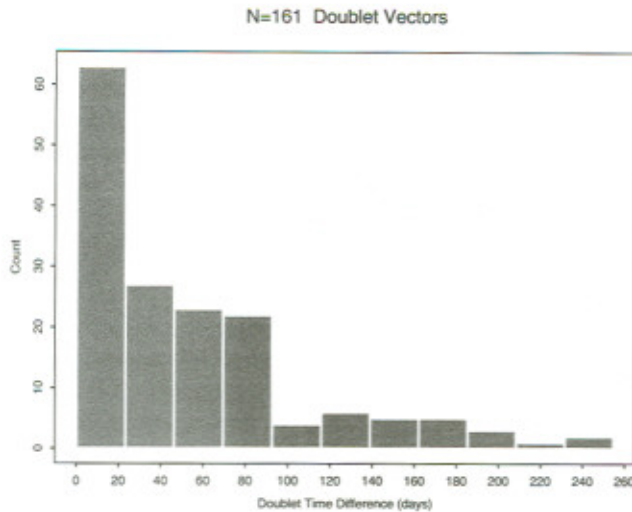
Figure 6. Histogram of 161 hypocenter pairs showing distribution of time intervals between doublets in the SW cluster. The great majority of events occur within a day of each other, although numerous doublets occur over periods of weeks and months.

The slope of the phase cross-spectrum provides an estimate of the time shift, where $\tau = \text{slope}/k$. In the example shown (Fig. 7), time window starts 0.1 sec before the onset of the P-wave arrival and extends 0.6 sec beyond. The time window must include a sufficient number of points for reliable spectrum estimates while not including too much extended, perhaps noisy, S-wave arrival and coda. Spectrum estimates of signals s_1 and s_2 are calculated using the multi-taper method (Lees and Park, 1995) with five 3π tapers. The multi-taper method provides a stable estimate of the coherency (Fig. 8) that is subsequently used to weight the phase cross-spectrum in determining the best linear fit slope.

Having estimated the slope τ, we can use relative phase shifts of one event with respect to another to find a high precision relocation vector. The relocation vector

$$\mathbf{r} = (\Delta x, \Delta y, \Delta z) \qquad (7)$$

is derived by linear inversion of the matrix equation,

$$\tau_i = \frac{\mathbf{r} \cdot \mathbf{n}_i}{\alpha} + t, \qquad (8)$$

where $\mathbf{n}$ is a vector along the ray path toward station i, t is an origin time correction, and α is the local velocity. For
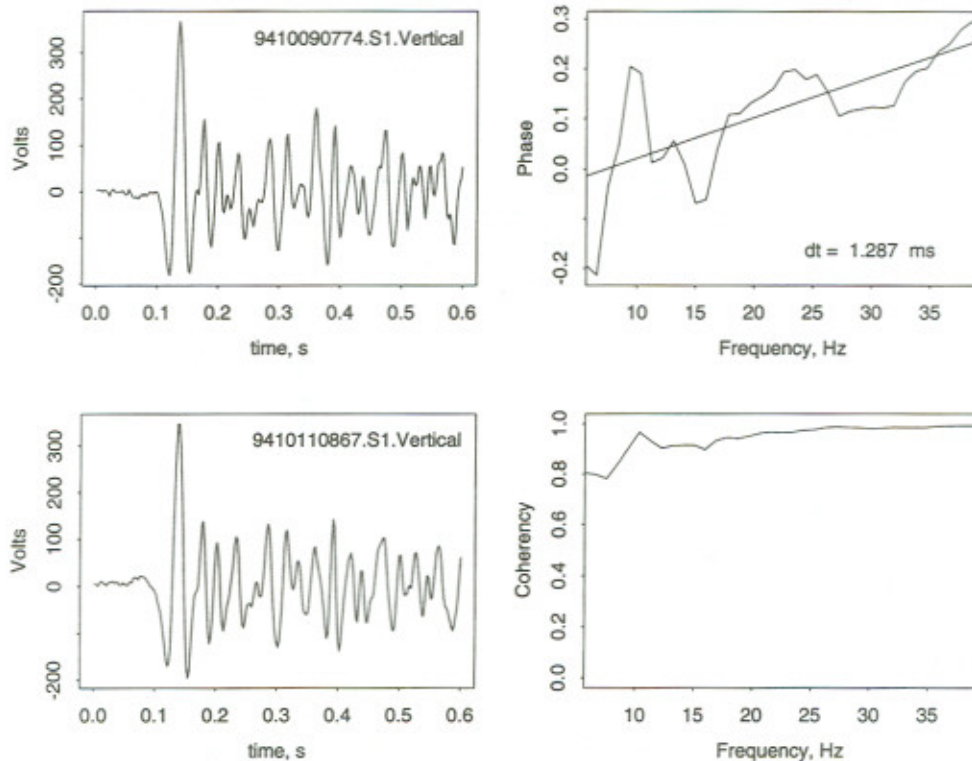

Figure 7. Station recording of a doublet event and cross phase analysis. Right-hand side shows the cross phase and the linear fit. The slope of the linear fit is phase shift of one signal relative to the other. Below is the cross-coherency as estimated by the multi-taper spectrum analysis. The cross-coherency is used to weight the cross phase spectrum for determining the phase shift.
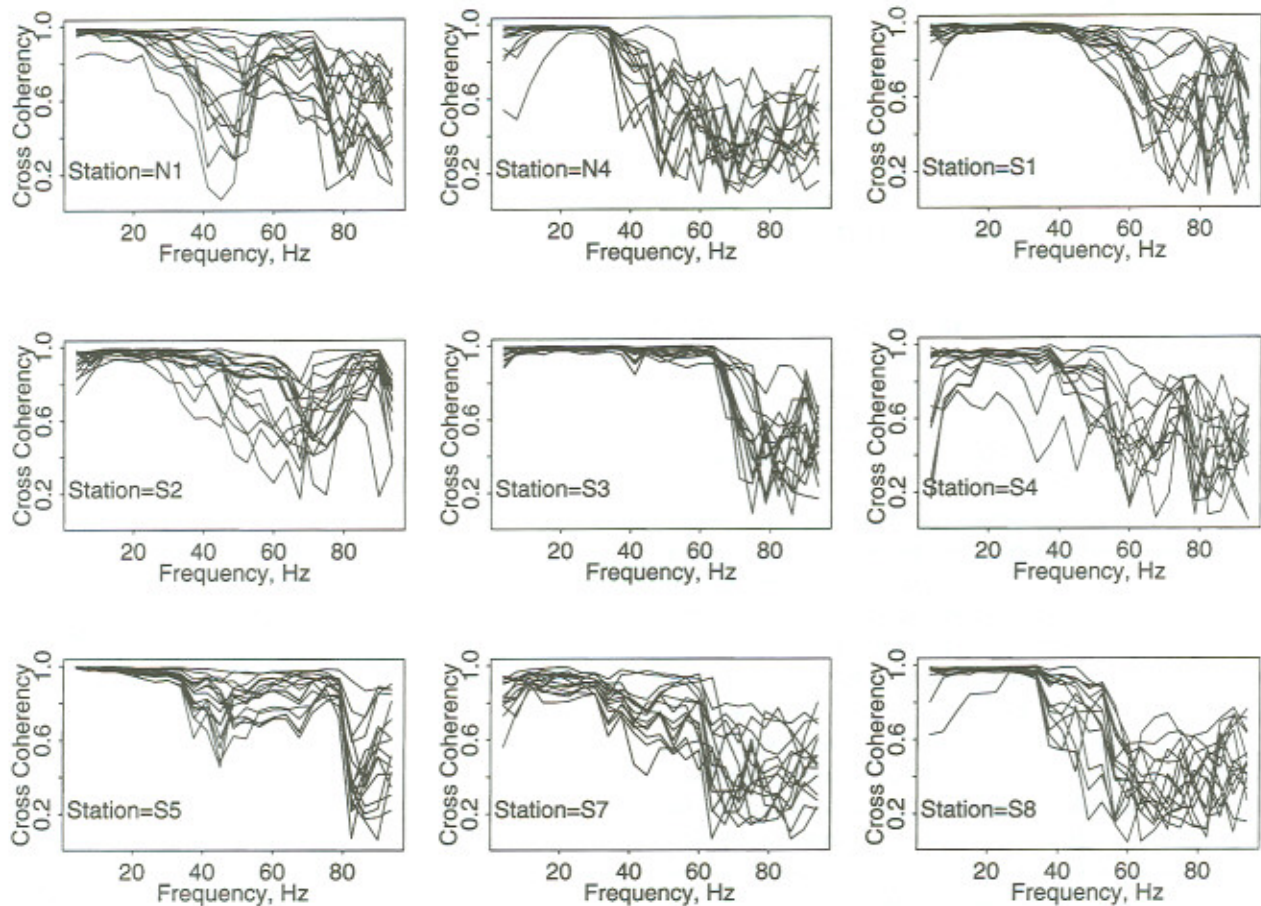
Figure 8. Cross-coherency plots for the NE1 cluster where the cross-spectrum of the master event is taken relative to the other events in the multiplet. There is some variability of coherency over the network, and some stations have significantly more noise than others. Station S1 (see Fig. 7), one of the best stations, appears to have very high coherency out to 45 Hz. The coherency curves are used to weight the cross phase spectra linear regression for determining relative phase shift.

multiplets, the event with the most recording stations is selected as a master, and each event in the multiplet is relocated relative to it. This procedure does not obtain absolute even location, but it does provide precise relative locations. We used several different master events in our relocation experiments; the results were for the most part consistent, although small differences were observed. Generally, the spatial orientations of events relative to each other were preserved, as illustrated in the example of Figure 9 where two different master events were chosen and resultant relocations are displayed. The overall orientations of the events remain consistent though the suite of events is shifted because of the different master.

The multiplet method for determining relative locations provides an assessment of error in equation (8). Because each estimate of relative phase shift is derived by linear regression of the cross phase spectrum, and this, in turn, is a weighted least-squares fit, a standard estimate of the covariance matrix for event location is easily derived. Each of the τ_i will have a corresponding uncertainty, estimated from the least-squares regression, which may be incorporated into inversion problem (8). A plot of the standard errors versus τ is provided in Figure 10. The τs are generally smaller than the sample rate, and the standard errors are smaller still. This analysis provides our relocation estimates with estimates of relative location error that are small, as seen in the next section. We note, however, that these simple estimates may be overly optimistic, as we have not adequately taken into account uncertainties in α or in $\mathbf{n}_i$. Because α is estimated at the master event, an error in velocity estimation merely adds a constant to the overall covariance analysis. Errors in $\mathbf{n}_i$ depend on the ray path, which depends on the full velocity model and the relative orientations of the stations with respect to the master. Here uncertainty estimates are likely to be different in horizontal versus vertical dimensions. While the local azimuthal direction of the emergent ray is probably well determined, the plunge or dip of the ray is more sensitive to local velocity uncertainties.

Because there is no formal method for determining the nonlinear relationship of model uncertainties and location error, we have resorted to a statistical sampling approach, akin to the "bootstrap" method. To estimate the influence of the velocity model on event relocations, we examine the distribution of potential locations from 100 randomly perturbed velocity models. To perturb the velocity models, a 20% perturbation was applied independently to each of the layers in the one-dimensional model. For each model, relative locations were calculated as described earlier, and all locations were saved for later examination. Figure 11 shows relative locations of two events in the NE1 cluster of events. The ellipsoids are the error estimates derived from inversion in equation (8). The plus symbols each represent an earthquake location relative to the master event (represented by a star) using a different velocity model. The bootstrap events cluster tightly around the location provided by the reference velocity model. This distribution shows a small horizontal spread (about 4 to 6 m) with a slightly larger spread in the vertical dimension (30 m). The spread generally stays within the bounds of the previously determined standard error based entirely on the inversion (equation 8). The fact that the relocations remain inside the previous error ellipsoids is arbitrary: a larger perturbation in velocity would make the distributions more diffuse. The choice of 20% velocity anomaly is not an unreasonable estimate—typical tomographic inversion analyses exhibit 10% fluctuations from background velocity models. These two estimates of uncertainty are independent and, most likely, uncorrelated. Spatial error bars derived from linear inversion are functions of data uncertainty, which in this case are determined from comparison of phase shifts in the time series. The phase shifts do not depend on the velocity model used for event location, although the relocation scheme does, and thus errors are correlated. If we assume they are uncorrelated, however, and add them together, we will obtain a conservative estimate of uncertainty. With this assumption, and observing that uncertainties associated with model errors are approximately equal to those estimated via inversion, we simply double the derived covariance matrix to estimate the error ellipsoid. Error ellipsoids represent a 1σ standard error, or a 68% confidence, assuming a Gaussian distribution. To see a 95% confidence bound, we must consider a 2σ ellipsoid (Figure 12). Combining all the multiplet data, we observed a mean 1σ deviation of $\sim$15 m with a maximum at $\sim$46 m and a minimum at $\sim$4 m.

An additional source of error may arise from the variable station distribution for each event. While it is difficult to determine precisely how this might affect the final result, we can provide a quantitative measure by examining the jackknife estimate of the variance of errors in each coordinate direction. The jackknife is a nonparametric method for estimating quantities such as standard deviation in situations when the underlying statistical distributions are unknown or analytically difficult to calculate (see Efron, 1982; Lees and Crosson, 1989; Tichelaar and Ruff, 1989; and for an ex-
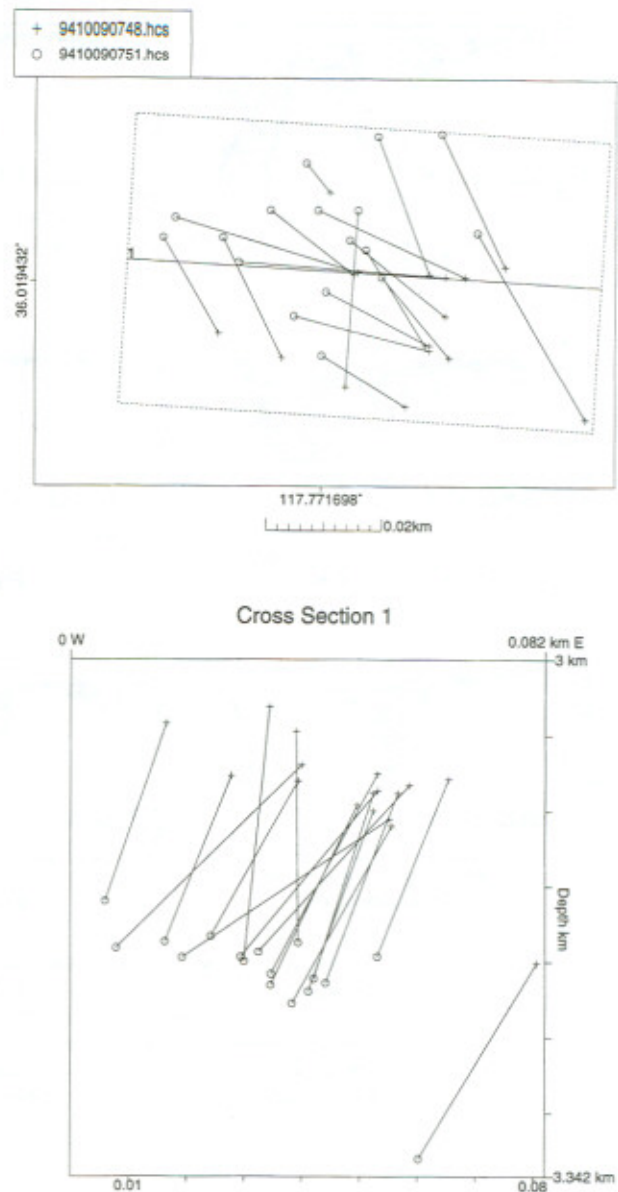

Figure 9. Plots showing shift of relocated events when a different master event is used. *Left:* Map view showing location of vertical cross section. *Right:* Vertical cross section. Events are projected onto the dashed line in the center of the selection box indicated on the left. The spatial pattern is fairly stable, and events generally shift in the same absolute direction. Master events are indicated by the larger, bold symbols. Circles are one sequence of relocation and plus marks are the alternative.

ample applied to earthquake location statistics, Iverson and Lees, 1996). The procedure involves repeating the relocation with the same master event, each time subsampling the data by deleting one station at a time. Results summarizing the standard deviations for each event in the three directions are presented in Figure 13. Among the 16 relocated events, we observe median errors of 17, 14, and 36 m in the east, north,
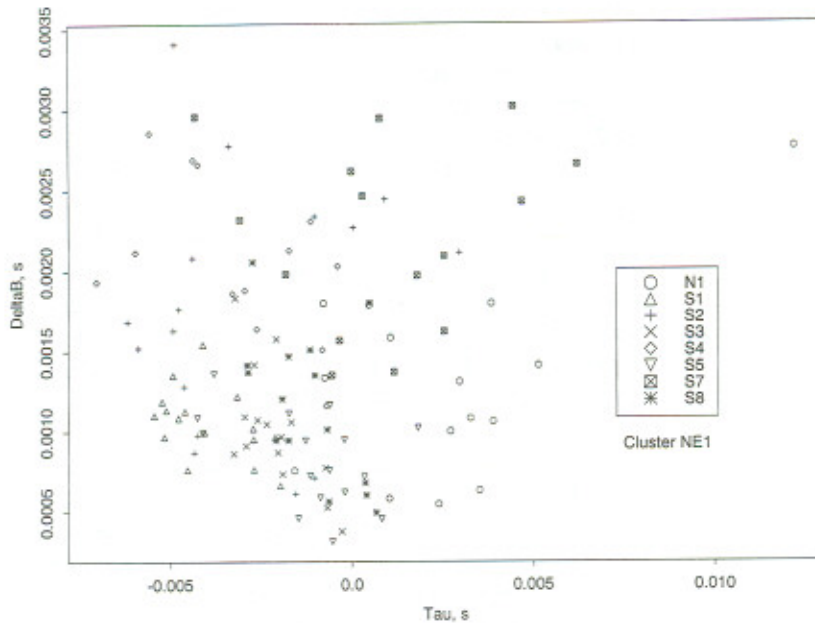
Figure 10. Plot of errors in time shifts as estimated by the error in the slopes of linear regressions of the cross phase spectra for cluster NE1. For each event and each station, the cross-spectrum of the master event and cluster events are calculated as in Figure 7. Errors of the slopes are estimated by the weighted least-squares regression and are passed on for use in the weighted relocation inversion.

and vertical directions, respectively. As in the discussion on errors introduced by velocity model errors, fluctuations of event relocations are on the order of 30 to 50 m in depth. A conservative approximation for errors in depth includes adding a 30-m error for model error, 30 m for fluctuations in station distribution, and 30 m for variation introduced in the phase shift estimation. The root mean square of these errors is 52 m, representing an average error based on all of the foregoing discussion. With these considerations in mind, we expect that, on average, our relocations are correct within ± 30 to 60 m at the 95% confidence level.

Results

Results showing relative locations of events using the relocation procedure for 17 events in cluster NE1 are presented in Figure 12a. The distribution of events in the NE1 cluster, including uncertainties, is over a 50 to 60-m area and extends about 200 to 300 m in depth. The spatial distribution suggests the events are located on a vertically elongated fault directed along one of the main fault directions observed in the surface geologic mapping for this region. The depth of the NE1 cluster is ~3 km, although the absolute location is not solved for in this analysis, because the cluster is located relative to the master event. On average, the resolution of the event relocation is one order magnitude better than the standard locations. Error ellipsoids of the relocated events are provided in Figure 12 and show that many of the events do not overlap, either horizontally or in depth. The time sequence of the events does not provide any significant insight—perhaps at this level and scale events occur on random locations on the fault plane. Hypocenters for the larger multiplets are presented in Figure 2 with closeups of the relocation sequences in Figure 12.

In plan view, the clusters typically enclose an area of

50 m^2 or less except for an occasional outlier. The spatio-temporal pattern of the events appears random: We do not observe an organization in the sequence of events in space. Rather, events seem to fluctuate spatially within the cluster volume without any clear temporal relationship. While it is tempting to suggest that the multiplets align along preferred fault directions, map view plots do not indicate this trend (Fig. 12). (Lines connecting events are for temporal analysis only and have no spatial significance. The wheel symbol is the first event of each sequence.) Table 3 provides the horizontal and vertical extent of all the clusters, showing that the clusters are similar in size. In all multiplet cases, the vertical distribution of events within each multiplet is significantly more pronounced than the horizontal scatter, suggesting that crack structures are elongated in depth.

Source parameters (moment, stress drop, corner frequency, and magnitude) used in this study were determined using spectral estimates of S-wave arrivals (Andrews, 1986; Alvarez, 1992). To determine source parameters for each event, S-wave arrival time windows were chosen by visual inspection for several arrivals per station. For each trace, Fourier amplitude spectra were calculated and the Andrews (1986) method was applied. Final source parameters were determined by averaging the independent estimates at each station. Fault rupture radii estimated from corner frequencies range from 30 to 80 m, with most events falling between 35 and 60 m (Fig. 14). High-resolution relative relocations generally show interevent distances considerably less than 40 m, suggesting either that events lie on the same fault patch or that they are reoccurrences of the same event.

Discussion

If clusters identified in this study represent true multiplets, that is, events rupturing the same fault repeatedly, we

Boot Strap Velocity Models

117.771851°

0.02km

Cross Section

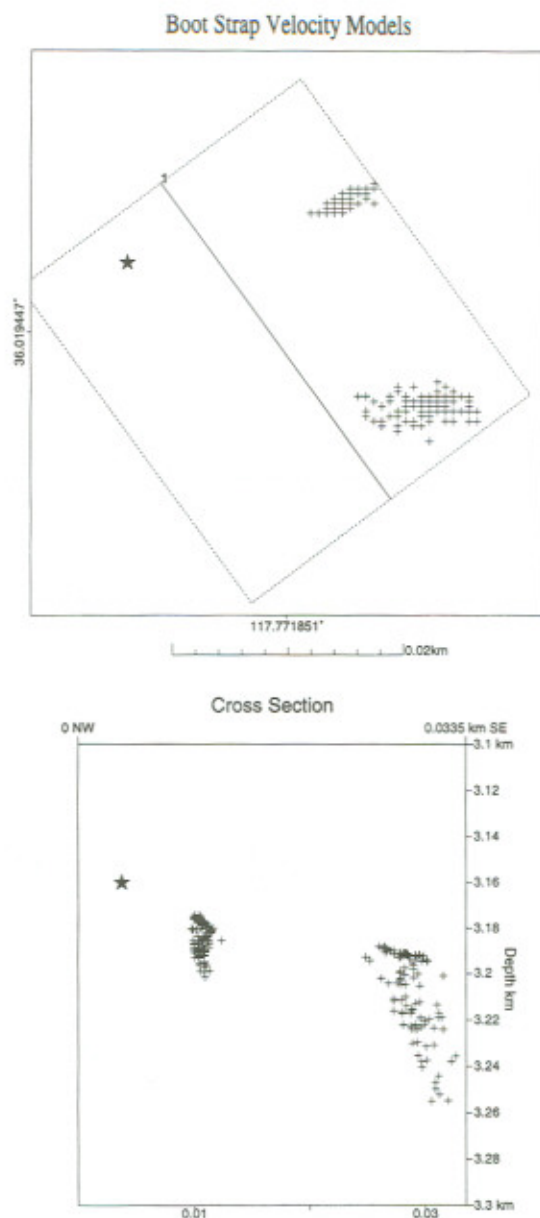0 NW   0.0335 km SE

Figure 11. Bootstrap estimation of sensitivity of event relocation to velocity models. 100 velocity models were generated and used to relocate two events (plus symbols) relative to the master (star).

would expect to see some form of fault healing, as observed along the Calaveras Fault in California (Marone *et al.*, 1995). However, we observe no evidence of any particular correlation of interevent lapse time and source parameters, such as stress drop or magnitude. The lack of such a correlation suggests either that the multiplets observed here are not repeating events or that they entail different physics than their larger counterparts. It may be that chemical processes involved in fault healing do not scale to such small events (magnitude >0) or that the presence of hydrofractures and hydrothermal fluid flow alters the process of fault healing

considerably. On the other hand, if these multiplets do not represent repeating events, we would not expect them to show correlations between lapse time and size. In this case, the high degree of similarity between events must be attributed to nearly identically oriented cracks distributed in a spatially restricted volume. For the 17 events in the NE1 cluster, the vertical distance spanning the whole multiplet is about 300 m. While adjacent events overlap, the full 300-m span suggests that separation between event multiplets is real; that is, it cannot be explained away by error ellipsoids produced in this study. Without installing more stations to observe new multiplets, we have no means for determining better locations than those derived in this study.

If we accept that these events are indeed distinct, that is, they occur on individual, nonoverlapping cracks, then multiplet clusters may provide a way to estimate crack density and orientation variations in the geothermal field. This hypothesis is predicated on the availability of a complete catalog, down to very small magnitudes, say M 1. Because the catalog may not be complete at this level, our approach may not be completely valid. It is entirely possible, however, that events on the lower end of the magnitude scale simply follow a different power-law relation than larger events (see Fig. 15). It has been suggested (Peter Malin, personal comm.) that the Coso microearthquake data are complete down to magnitude M 0.5. The Gutenberg–Richter plot shows that b-values change linearly below M 1.5 and in particular in the range between -0.5 and 1.5 where multiplet events are observed. Still, the question of catalog completeness remains open, and there is a possibility that multiplets do not represent complete sequences. Using the Gutenberg–Richter relationship defined by Figure 15, we estimate that, assuming the catalog is complete between magnitudes 1 and 3, and the linear law holds, there is a deficit of events ranging from a factor of 6 to 16-fold. Therefore, estimates of density based on counting of events should increase accordingly, although this approach rests on assumptions that may be as questionable as failing to make any adjustment.

We can approximate the NE1 cluster volume by taking the spread of the events in each of three dimensions and forming their product, $V = 263,590$ m^3 (see Table 3). The NE1 cluster includes 17 events, each with fracture radius derived from corner frequencies f_c and local shear-wave velocity $v = 3.0$ km/sec,

$$r = \frac{2.34v}{2\pi f_c} \qquad (9)$$

(see Andrews, 1986). The total fracture area for the volume is $A = \sum_{i=1}^{N} \pi r_i^2 = 114,721$ m^2, which gives a fracture density of FD $= A/V = 0.425$. This may be an overestimate if we have overestimated fracture radius from corner frequency neglecting attenuation effects and slightly underestimated cluster volume. On the other hand, if we assume that each of the $N = 17$ events in the NE1 multiplet has a char-
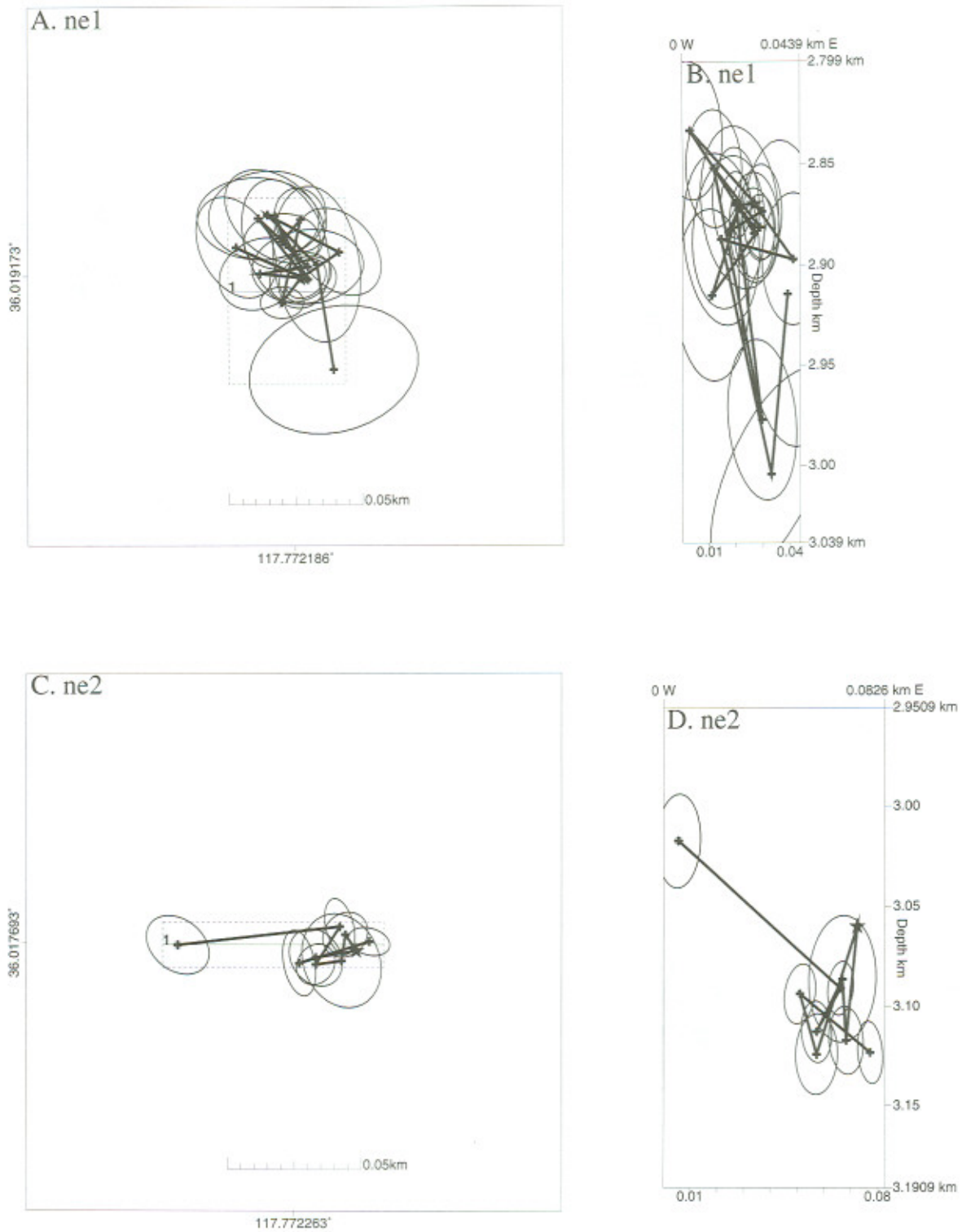
Figure 12. Close up of seven thumbnail boxes shown in Figure 2. Each sequence is shown as a connected line with a wheel symbol indicating the first event of the series. Earthquakes are plotted as plus marks at vertices of a vector connecting all the events in chronological order. Diamonds are locations of events using single-event location scheme, that is, are nonrelative locations. Error ellipsoids are plotted on horizontal and vertical projections using 2 σ ellipsoids (95% confidence) including effects of model error. The star is the reference (master) event, and the wheel is the first event in the time sequence.
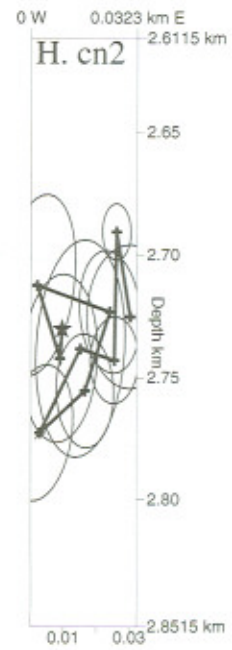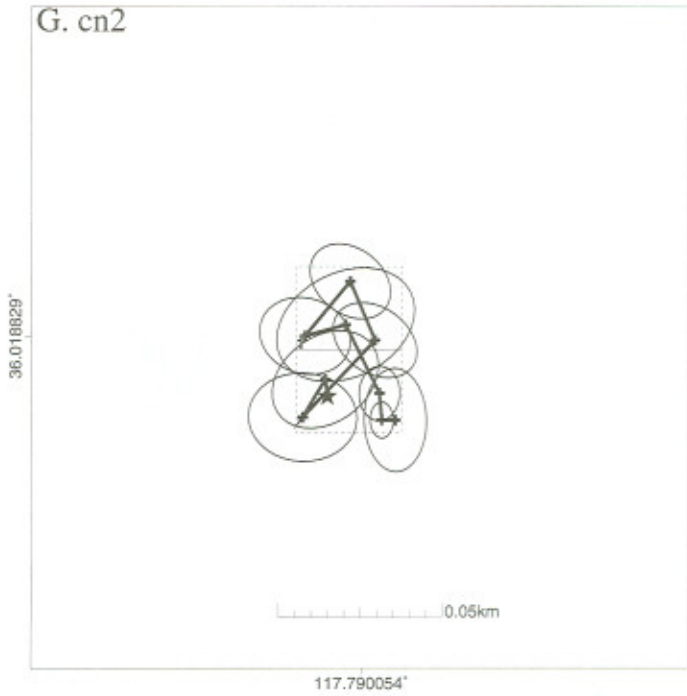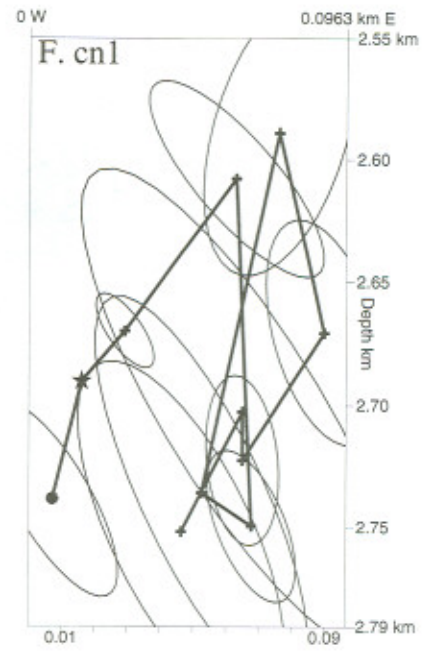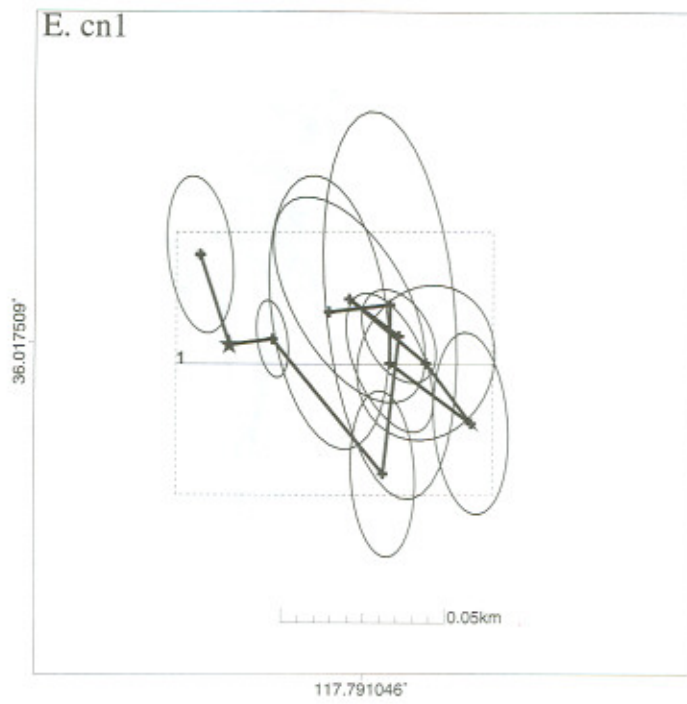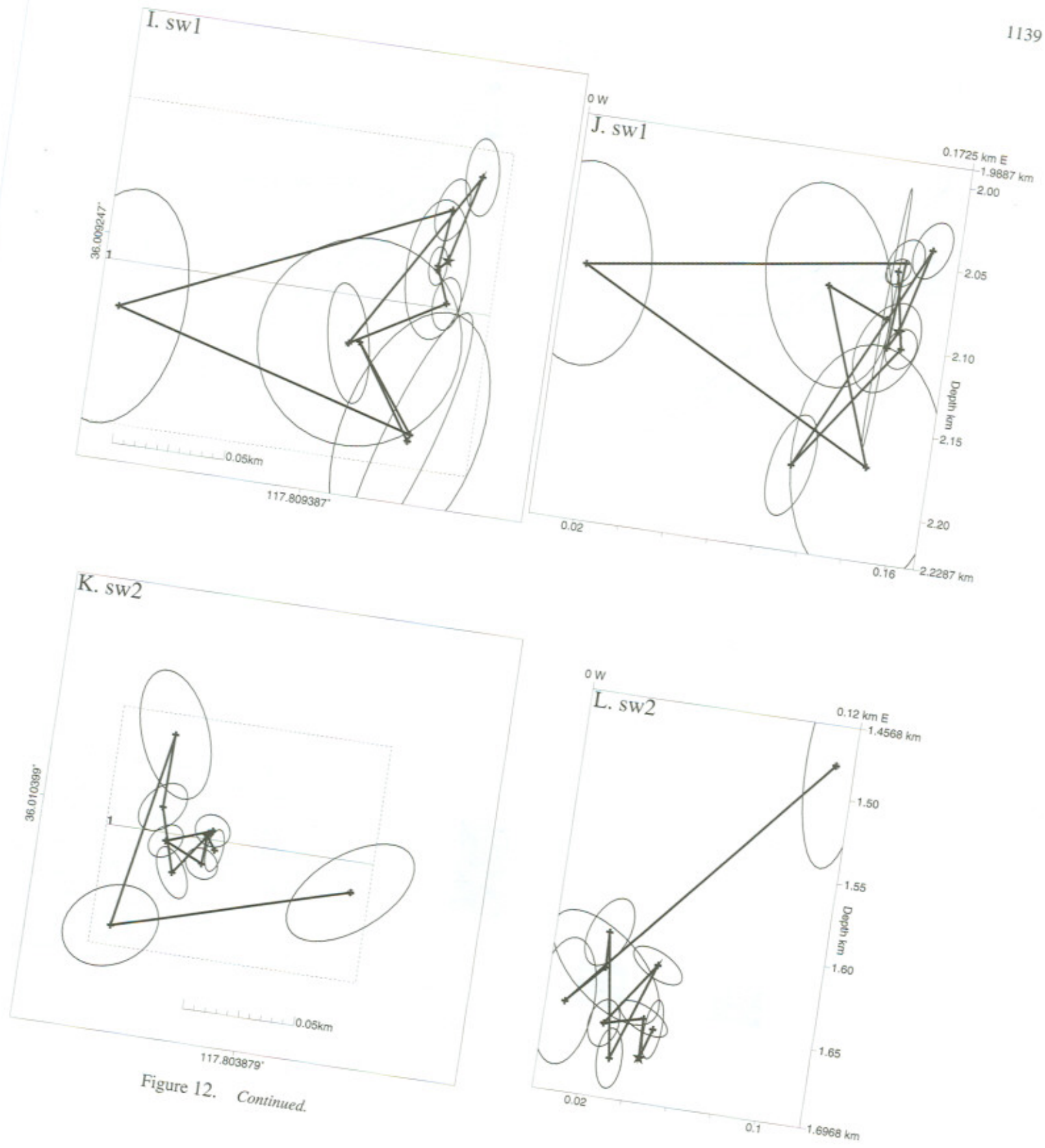
Figure 12. *Continued.*
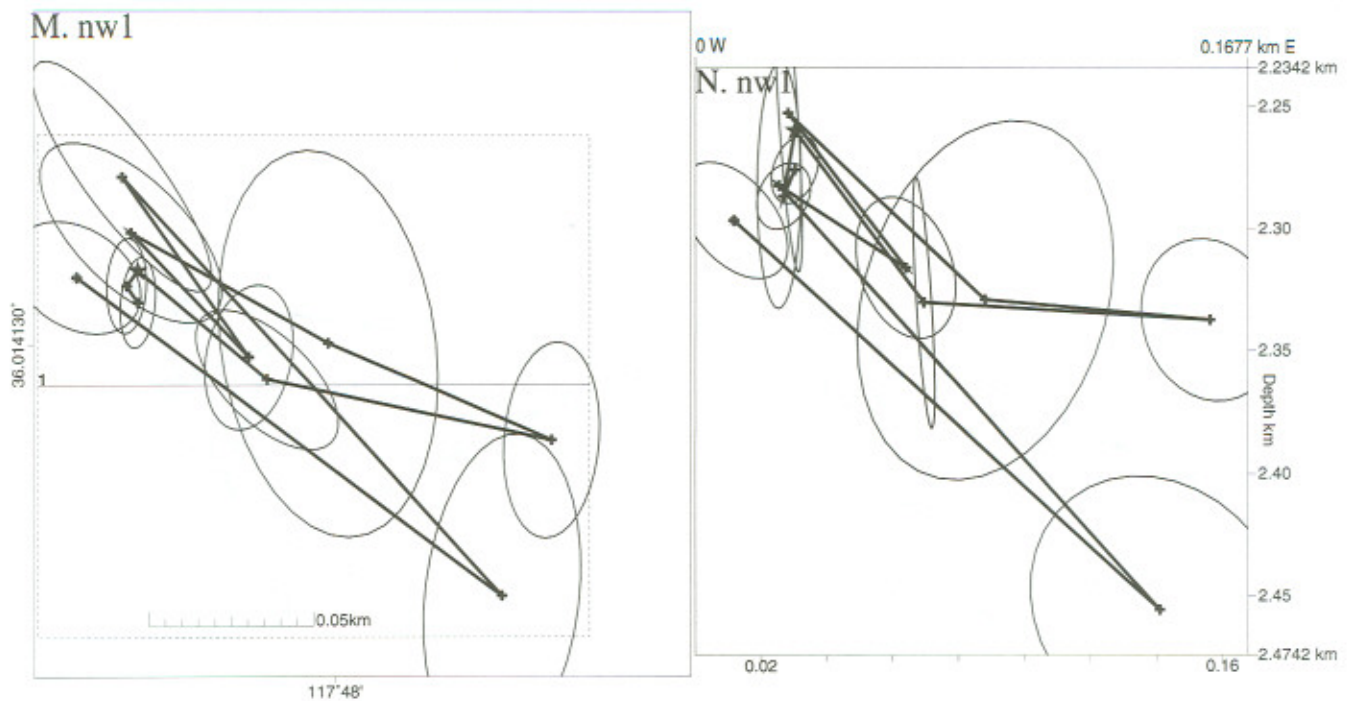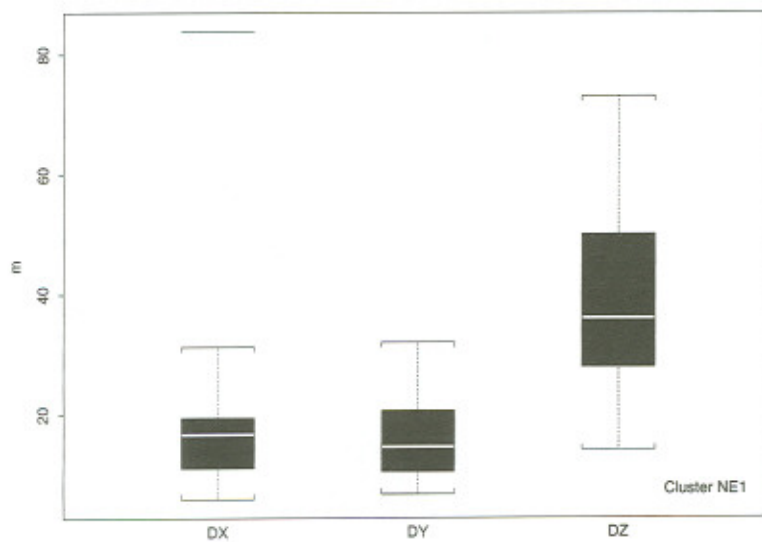
Figure 12. Continued.

Figure 12.   *Continued.*

Figure 13.   Box plots showing distribution of estimated station jackknife errors in the east–west (DX), north–south (DY), and vertical (DZ) coordinate dimensions. Box plots show the median (white line) interforth quartiles (shaded region), octiles (whiskers), and outliers (bars). There is one outlier in the DX direction at 79 m. Median values summarize expected errors associated with station distribution for the spatial three dimensions. Errors in the vertical direction are on average approximately twice as high as in the horizontal directions.
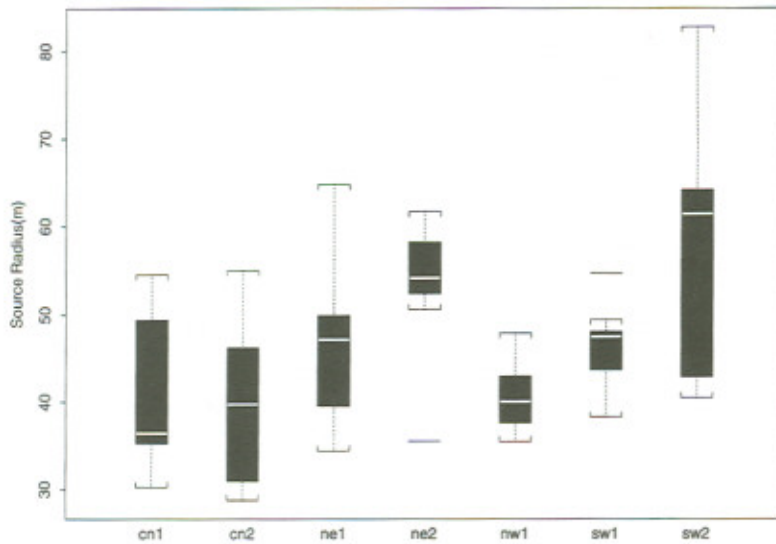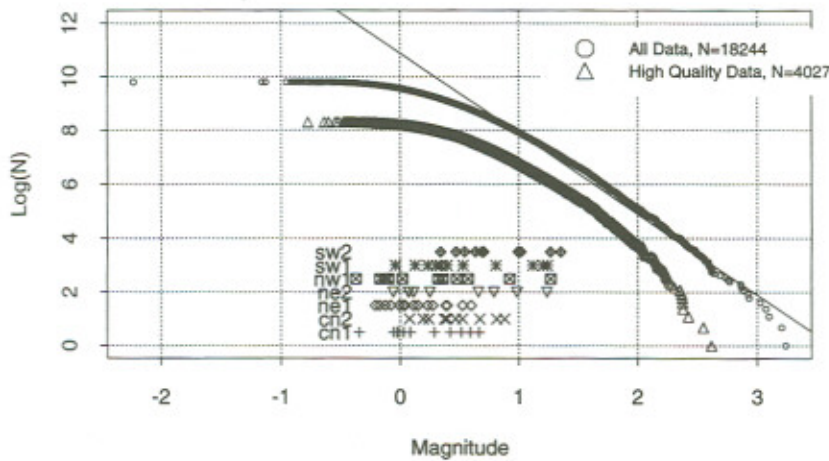
Figure 14. Box plots showing distributions of multiplet source radii. Radius units are in meters, and labels refer to the multiplet tags and geographic regions. Box plots are described in Figure 13.

Gutenberg-Richter plot of Coso Micro-Earthquakes
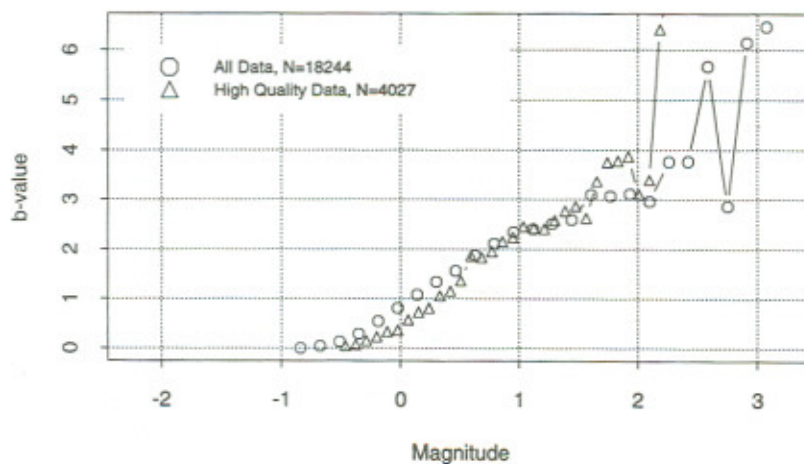

b-values for Coso Data

Figure 15. (*Top*) Gutenberg–Richter plot showing log number of events greater than a given magnitude versus magnitude. Circles are the full data set (18,244 events), triangles are high-quality locations (4027 events), and the diamonds represent the multiplet events plotted on the zero line for reference. The straight line is used to evaluate deficits in event density estimates. (*Bottom*) b-values as a function of magnitude for the data in the plot above. Generally, b-values increase linearly to magnitude 1.0 to 1.5 where leveling is apparent for a short interval.

Table 3

Calculated parameters from specific multiplets. The area is the sum of all fracture surfaces assuming circular cracks with radii estimated from corner frequency.

Cluster	Number	Dx (m)	Dy (m)	Dz (m)	Vol (m³)	Area (m²)	FD (1/m)	Dt (d)	FI (1/m/d)
cn1$_i$	11	66.0	82.5	162.6	885,283	56,455	0.064	263.1	0.00024
cn2$_i$	10	41.9	28.2	82.0	97,068	52,950	0.545	206.4	0.0026
ne1$_i$	17	57.6	39.9	171.1	393,485	114,721	0.292	106.7	0.0027
ne2$_i$	9	14.0	71.5	106.7	106,601	82,487	0.774	9.4	0.082
nw1$_p$	11	126.5	144.4	202.6	3,701,626	56,527	0.015	320.4	4.8e-.05
sw1$_p$	11	120.3	151.4	138.2	2,515,761	74,575	0.030	224.7	0.00013
sw2$_i$	10	88.1	103.1	192.2	1,746,372	109,055	0.062	119.1	0.00052
ne1*	16	32.2	39.9	171.1	219,866	11,011	0.505	11.7	0.043

Fracture density (FD) is the ratio of the sum of the fracture surface areas to the total volume, and fracture intensity (FI) is the density divided by the time span (Dt). The second NE1 line on the bottom represents parameters calculated when the last event of the NE1 sequence, which occurred 100 days after its corresponding preceding event, is removed. Subscripts (i) and (p) refer to cluster proximity to injection or production wells, respectively.

acteristic radius of $r = 30$ m, a lower bound, our estimate of fracture density, measured by taking the ratio of fracture surface area $(N \times \pi r^2)$ over a generic volume estimate of $V = 30 \times 30 \times 300$ m³, is 0.178 m²/m³. Taking into account the time for the multiplet to occur (DT = 106 days), we arrive at a fracture intensity FI = 0.0041 m^{-1} d^{-1}, representing a time-averaged fracture density. Because one event in the NE1 cluster has occurred more than 94 days after the previous event, and the full span of the first 16 events is only 11 days, it may be useful to examine just the first 16 events and consider them as a separate (reduced) cluster, which we designate NE1*. The last row of Table 3 (NE1*) shows that the fracture density (FD) does not change significantly when we remove the outlying event but the fracture intensity (FI) changes by one order of magnitude. Table 3 lists similar calculations for other clusters in the Coso data set. Fractures NE1* and NE2 have the shortest time spans and corresponding largest FIs and are apparently associated with fluid injection (Frank Monastero, personal comm.). Multiplets NW1 and SW1 have the smallest FDs and FIs and are located closer to production wells (rather than injection wells), in contrast to the other multiplets. It appears that proximity to injection increases FD and FI by 10 to 100 times. Finally, we should point out that if we have excluded events, our estimates will be biased. In this case, we are most likely underestimating the number of fractures in any given volume, so estimates of fracture density represent lower bounds. For density estimates, an approximate factor of 10 increase (see previous text and Fig. 15) for all clusters might be an appropriate way to compensate for this bias.

Previous studies used tomographic backprojection of split shear-wave time differentials to estimate crack density at Coso (Shalev and Lou, 1995; Lou and Rial, 1997). Their results suggest there is a low crack density below station S6 extending to at least 3.5 km depth. This region has considerably less seismicity than surrounding blocks. The fracture and multiplet analyses presented here do not sample this region directly, as multiplets NE1 and NE2 are south of station S6. These clusters seem to coincide with the sharp gra-

dient in the anisotropy results, although no signal of elevated crack density is apparent in Shalev and Lou's (1995) work near NE1. It is possible that the spatially and time averaged anisotropy analysis is not sensitive to recent fractures, as is the multiplet analysis. Anisotropy analysis may be particularly sensitive to microcracks and dilatency, which are not observed in the present study of fractures. It is, therefore, not obvious that the two analyses must agree. However, the areas where multiplets occur at Coso coincide with areas that exhibit elevated anisotropy. Estimates of crack density from the tomographic study differ from the multiplet density estimates by approximately a multiple of 10. [In this article, we measure fracture density as area over volume. Crack density measured by Shalev and Lou (1995) is represented as a nondimensional number. If one multiplies the FD values in Table 3 by a typical crack length (10 to 30 m), the values are 10 to 100 times greater than the average 0.035 value estimated for crack density by Shalev and Lou.] Because of the effects of regularization and damping, however, we do not place high confidence in the absolute value of crack density obtained from tomographic inversion.

Conclusion

Multiplet analysis of Coso geothermal microseismicity shows discrete, nearly vertical faults or rupture zones where multiple hypocenters originate. These similar events exhibit a wide range of timescales spanning seconds to years. In one case, as many as 16 events occurred in a short timescale (less than one month), delineating cracks or faults activated by changes in stress, most probably due to fluid injection. A relative relocation procedure provides hypocenter estimates with 30 to 60-m resolution and orients events in distinct clusters most likely associated with preexisting cracks activated by hydrothermal flow. The data do not allow us to determine whether these events are true repeated events or simply a set of similarly oriented cracks rupturing randomly in time. Because the events seem to be separated by more than the estimated rupture radius, however, I conclude that

Coso multiplets most likely represent swarms of small, nearly identically oriented cracks activated by fluid-pressure fluctuations. Careful recording of multiplets such as these, where catalogs are guaranteed to be complete to a relatively low magnitude, may provide estimates of variation of crack density and orientation in the geothermal field.

Acknowledgments

References

Alvarez, M. (1992). The seismotectonics of the southern Coso range observed with a new borehole seismograph network, *Master's Thesis*, Duke University, 152 pp.

Andrews, D. J. (1986). Objective determination of source parameters and similarity of earthquakes of different size, in *Earthquake Source Mechanics*, S. Das, J. Boatwright, and C. Scholz, (Editors), *Am. Geophys. Union Monograph 37*, Vol. 6, 259–267.

Aster, R. and J. Scott (1993). Comprehensive characterization of waveform similarity in large microearthquake data sets, *Bull. Seism. Soc. Am.* **83**, 1307–1314.

Duffield, W. A. and C. R. Bacon (1981). Geologic map of the Coso volcanic field and adjacent areas, Inyo County, California, U.S. Geol. Surv. Misc. Invest. Series, MAP-1200.

Duffield, W. A., C. R. Bacon, and G. B. Dalrymple (1980). Late Cenozoic volcanism, geochronology and structure of the Coso Range, Inyo County, California, *J. Geophys. Res.* **85**, 2381–2404.

Efron, B. (1982). *The Jackknife, the Bootstrap and Other Resampling Plans*, Society for Industrial and Applied Mathematics, Philadelphia, 92 pp.

Feng, Q. and J. M. Lees (1998). Microseismicity, stress, and fracture within the Coso geothermal field, California, *Tectonophysics*, **289**, 221–238.

Fremont, M.-J. and S. D. Malone (1987). High precision relative locations of earthquakes at Mount St. Helens, Washington, *J. Geophys. Res.* **92**, 10223–10236.

Gillard, D., A. M. Rubin, and P. Okubo (1996). Highly concentrated seismicity caused by deformation of Kilauea's deep magma system, *Nature* **384**, 343–346.

Haase, J. S., P. M. Shearer, and R. C. Aster (1995). Constraints on temporal variations on velocity near Anza, California, from analysis of similar event pairs, *Bull. Seism. Soc. Am.* **85**, 194–206.

Iversen, E. S. and J. M. Lees (1996). A statistical technique for validating velocity models, *Bull. Seism. Soc. Am.* **86**, 1853–1862.

Lees, J. M. and R. S. Crosson (1989). Tomographic inversion for three-dimensional velocity structure at Mount St. Helens using earthquake data, *J. Geophys. Res.* **94**, 5716–5728.

Lees, J. M. and J. Park (1995). Multiple-taper spectral analysis: a stand-alone C-subroutine, *Comput. Geol.* **21**, 199–236.

Lou, M. and J. A. Rial (1997). Characterization of geothermal reservoir crack patterns using shear-wave splitting, *Geophysics* **62**, 487–494.

Marone, C., J. E. Vidale, and W. L. Ellsworth (1995). Fault healing inferred from time dependent variations in source properties of repeating earthquakes, *Geophys. Res. Lett.* **22**, 3095–3098.

Nadeau, R., M. Antolik, P. Johnson, W. Foxall, and T. V. McEvilly (1994). Seismological studies at Parkfield III: microearthquake clusters in the study of fault-zone dynamics, *Bull. Seism. Soc. Am.* **84**, 247–263.

Phillips, W. S., L. S. House, and M. C. Fehler (1997). Detailed joint structure in a geothermal reservoir from studies of induced microearthquake clusters, *J. Geophys. Res.* **102**, 11745–11763.

Poupinet, G., W. L. Ellsworth, and J. Frechet (1984). Monitoring velocity variations in the crust using earthquake doublets: an application to the Calaveras Fault, California, *J. Geophys. Res.* **89**, 5719–5731.

Roquemore, G. (1980). Structure, tectonics, and stress of the Coso Range, Inyo County, California, *J. Geophys. Res.* **85**, 2434–2440.

Shalev, E. and M. Lou (1995). Tomographic inversion for crack-density in Coso, California, *EOS* **76**, 351.

Tichelaar, B. W. and L. J. Ruff (1989). How good are our best models: jackknifing, bootstrapping and earthquake depth, *EOS* **70**, 593.

Vidale, J. E., W. L. Ellsworth, A. Cole, and C. Marone (1994). Variations in rupture process with recurrence interval in a repeated small earthquake, *Nature* **368**, 624–626.

Wu, H. and J. M. Lees (1996). Attenuation structure of Coso geothermal area, California, from P wave pulse widths, *Bull. Seism. Soc. Am.* **86**, 1574–1590.

Department of Geology and Geophysics
Yale University
P.O. Box 208109
New Haven, Connecticut 06520-8109